Nano Energy 150 (2026) 111780

Contents lists available at ScienceDirect

Nano Energy

journal homepage: www.elsevier.com/locate/nanoen

Full paper

Evaporative hydrogels for high-performance ambient body heat harvesting via thermoelectric

Zichen Gong [a], Jinfeng Dong [b], Soe Ko Ko Aung [c], Thang Bach Phan [d,e], Qi Qian [a], Tosawat Seetawan [f], Surasak Ruamruk [g], Yujie Ke [h], Bhuvanesh Srinivasan [i], Zhaogang Dong [j], Sai Kishore Ravi [k], Ady Suwardi [a,*], Jing Cao [l,m,**]

[a] Department of Electronic Engineering, and Shun Hing Institute of Advanced Engineering, The Chinese University of Hong Kong, Sha Tin, New Territories, Hong Kong SAR 999077, China
[b] School of Materials Science and Engineering, Nanyang Technological University, 50 Nanyang Ave, 639798, Singapore
[c] Department of Physics, Materials Research Laboratory, University of Mandalay, Mandalay 05032, Myanmar
[d] University of Health Sciences, Ho Chi Minh City 700000, Viet Nam
[e] Vietnam National University, Ho Chi Minh City 700000, Viet Nam
[f] Program of Physics, Faculty of Science and Technology, Sakon Nakhon Rajabhat University, 680 Nittayo Rd., Mueang District, Sakon Nakhon 47000, Thailand
[g] Thermoelectric Research Laboratory, Center of Excellence on Alternative Energy, Research and Development Institution, Sakon Nakhon Rajabhat University, 680 Nittayo Road, Mueang District, Sakon Nakhon 47000, Thailand
[h] School of Interdisciplinary Studies, Lingnan University, Tuen Mun, Hong Kong, China
[i] Thermal Energy Materials Group, Department of Metallurgical and Materials Engineering, Indian Institute of Technology Madras (IIT-Madras), Chennai 600 036, India
[j] Singapore University of Technology and Design, Singapore 487372, Singapore
[k] School of Energy and Environment, City University of Hong Kong, Hong Kong 999077, China
[l] Institute of Materials Research and Engineering, Agency for Science, Technology and Research, 2 Fusionopolis Way, 138634, Singapore
[m] Department of Materials Science and Engineering, National University of Singapore, Singapore 117574, Singapore

ARTICLE INFO

Keywords:
Thermal impedance
Evapolectrics
Thermoelectrics
TEG
Water evaporation
Energy harvesting

ABSTRACT

The increasing demand in power of modern environmental and health sensors have spurred the development of ambient energy harvesting to reduce reliance in battery. Thermoelectric generators (TEGs) are a promising technology, which convert waste or body heat into electricity. However, their power output is severely limited by the thermal impedance mismatch, particularly between the human skin and TEG interface. This work introduces a novel approach to overcome this limitation by integrating a hydrogel into the TEG system. It has been revealed that the enthalpy from the hydrogel's water evaporation effectively achieves thermal impedance matching while simultaneously maximizing the heat flux. Furthermore, by optimizing the TEG's fill-factor, we increased the power density by nearly two orders of magnitude compared to conventional TEG systems. As a proof of concept, our device combined body heat with hydrogel evaporation using an optimized fill-factor of 0.48 (using 52 % less material). This setup achieved a power density of 150 μWcm^{-2}, which was sufficient to power four wireless sensors. This work demonstrates a counter-intuitive synergistic benefit, that is achieving superior thermal matching while significantly reducing thermoelectric material usage. Our findings redefine optimization approach for TEGs and offer a viable pathway toward realizing off-grid, self-powered sensors.

1. Introduction

The advent of sensors and electronics has revolutionized health and environmental monitoring, offering unprecedented opportunities with real-time data and personalized insights. Over the years, these devices have evolved rapidly, propelled by expanding functionalities such as continuous vital sign monitoring, sweat analysis, motion detection, personal thermal regulation, and environmental parameter assessment [1–9]. This evolution comes at the cost of increased power consumption, posing significant challenges to their practicality and widespread

* Corresponding author.
** Corresponding author at: Institute of Materials Research and Engineering, Agency for Science, Technology and Research, 2 Fusionopolis Way, 138634, Singapore.
E-mail addresses: asuwardi@ee.cuhk.edu.hk (A. Suwardi), caoj@nus.edu.sg (J. Cao).

https://doi.org/10.1016/j.nanoen.2026.111780
Received 13 November 2025; Received in revised form 1 February 2026; Accepted 4 February 2026
Available online 5 February 2026

adoption [2,10,11]. Owing to their finite lifespan and environmental footprint, traditional reliance on batteries has driven the scientific community to explore sustainable alternatives through ambient energy harvesting [12–19].

The human body, as a natural heat source, dissipates approximately 60–100 W (30–50 Wm^{-2}) of thermal energy depending on activity level, making it an attractive reservoir for energy harvesting. Thermoelectric generators (TEGs), which convert temperature gradients (ΔTs) into electrical energy, have emerged as promising solutions for converting this ever-present heat into electricity for self-sustaining systems [19–24]. Innovative use of TEG such as cyclic thermal regulation, module design, and 3D printed structures have also been reported [24–28]. Over the years, the performance of thermoelectric (TE) materials has improved drastically [29–37]. Despite this, the efficiency of TEGs for body heat harvesting continues to be hampered by significant thermal impedance at critical interfaces between the skin-TEG and the TEG-ambient [20]. These parasitic thermal impedances often dominate the system, reducing the effective ΔT across the thermoelectric material and limiting the power output. Compounding this challenge is the inherently limited thermal output of the human body. Unlike industrial applications, where ΔTs can exceed hundreds of degrees, TEGs for body heat harvesting have narrow operating temperatures (approximately 32–35°C) between the skin and ambient air. In addition, heat dissipation to the ambient environment is particularly challenging, necessitating a bulky heat sink, as illustrated in Fig. 1a. Researchers have also investigated flexible TEGs to conform to the body's contours, although this approach only marginally improves thermal coupling [20]. As a result, power densities have remained modest, with one of the highest reported values under realistic conditions reaching 0.184 Wm^{-2} [38]. This output, while notable, falls short of the requirements of many wearable electronic devices [2,10].

Our research addresses these limitations by introducing a different approach building on our preceding works on evapolectrics [39,40]. We integrate bodily heat flux with the evaporative cooling effect via water evaporation from the hydrogel. This design is inspired by natural human body temperature regulation via sweat evaporation, which can provide a water supply for hydrogels. This synergy markedly amplifies the ΔT across the TEG beyond conventional heat sink limits, as shown in Fig. 1b. Hydrogels, known for their high water content and tunable properties, have been employed in thermal regulation and energy applications [39,41–43]. By leveraging the water evaporation enthalpy from the hydrogel, our system effectively dissipates heat to the ambient environment, counteracting the thermal impedance that typically constrains TEGs [20]. Furthermore, this allows us to optimize the fill factor (*FF*, defined in this work as the ratio of the TEG area to the hydrogel or device area) to achieve thermal impedance matching across the system, which is a critical factor in maximizing the power output. Consequently, a power output of 7.5 mW and a power density of 1.5 Wm^{-2} were achieved, which are 2-order-of-magnitude greater than the power density of typical TEG benchmarks and close to an order of magnitude higher than the record power density of wearable TEG [2,38]. This energy is sufficient to perpetually power four wireless environmental sensors capable of round-the-clock monitoring. Remarkably, the highest power level (189 % higher than non-optimized setup) with the optimized *FF* was achieved with 52 % fewer materials, 79 % thinner, and 63 % lighter devices. This superior performance with less material highlights the synergy between hydrogel-enhanced evaporative cooling and optimized *FF*.

As shown in the Fig. 2a radar chart, the hydrogel-enhanced TEG outperforms the conventional design across all key metrics: weight, heat flux, power output, thickness, and ΔT. This superior performance stems from the synergy between hydrogel evaporative cooling and an optimized ratio of active TEG to evaporation surface, yielding higher power output with reduced material usage. Fig. 2b presents a logarithmic scale benchmark of power density in this work against previously reported ambient energy harvesting systems. The evaporation-enhanced TEG

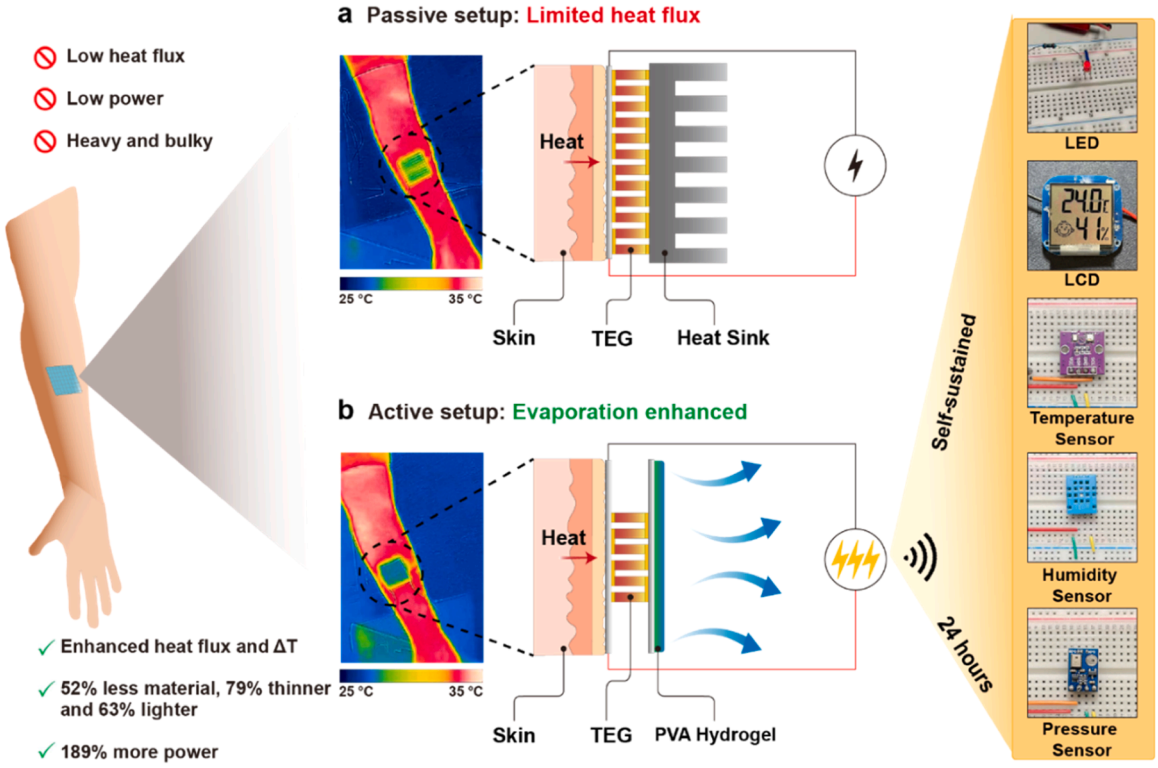

Fig. 1. Comparison of traditional and evaporation-enhanced TEG configurations. (a) Traditional setup with a passive heat sink, where thermal imaging indicates limited heat dissipation. (b) Evaporation-enhanced setup integrating a hydrogel and optimized fill factor (FF). This design improves heat dissipation, increasing power output by 189 % while reducing material usage by 52 %, thickness by 79 %, and weight by 63 % for continuous wireless sensing.

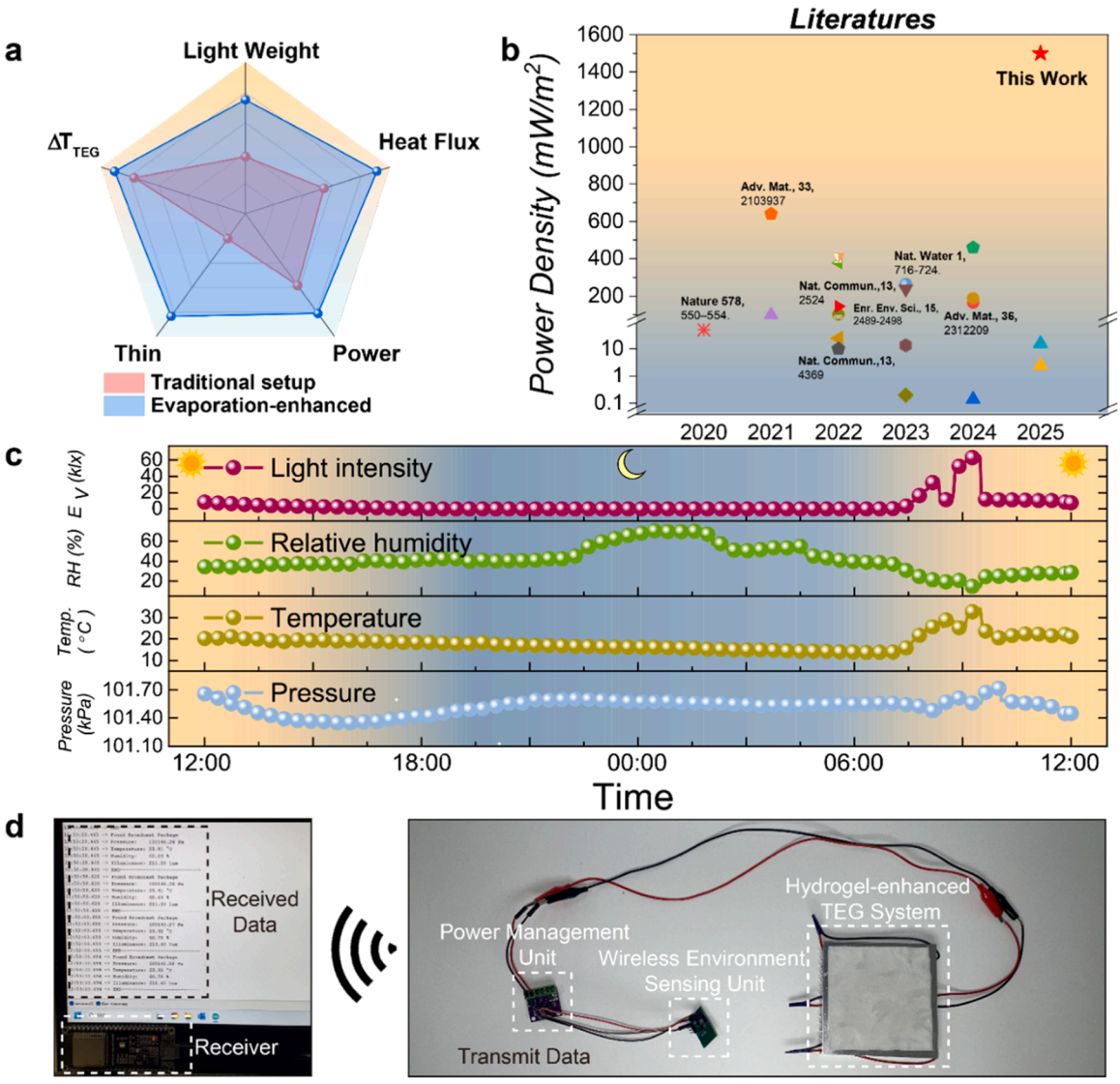

Fig. 2. (a) Radar chart comparing between traditional and evaporation-enhanced TEGs. (b) Power density benchmark against state-of-the-art ambient energy harvesters. (c) Continuous 24-hour environmental data powered by the 10 × 10 cm hydrogel-TEG system. (d) Photograph of the integrated self-powered wireless sensing unit (light, temperature, humidity, pressure).

achieves a power density of 1.5 W/m^2, surpassing traditional evaporation-based systems (hydrovoltaics) without external energy input and many other photothermal systems reliant on external thermal/light inputs [44]. To demonstrate the application of self-sustaining sensors, a representative setup mimicking the amount of heat flux from an evaporation-enhanced TEG was prepared to simultaneously energize four sensors over a 24-hour period, as shown in Fig. 2c. This enables continuous monitoring of key environmental parameters and underscores the system's potential for off-grid energy applications, particularly in environments with limited sunlight and heat. The real image of the device is shown in Fig. 2d, showing PVA hydrogel-TEG connected to a nano power unit and wireless sensors.

On a fundamental level, this work demonstrates the advantages of evaporation-enhanced TEGs over traditional TEGs, potentially driving further fundamental exploration in maximizing evaporation rate, for instance, through thin liquid film evaporation. Technologically, by overcoming the longstanding barriers of thermal impedance and limited body heat, this work potentially helps to advance self-sustained sensors, paving the way for next-generation devices that are both autonomous and multifunctional.

2. Enhanced heat flux from hydrogel evaporation

To understand the role of the hydrogel in enhancing the power output, Fig. 3a shows a comparison of the temperature profile across the human body, skin-to-TEG interface, TEG, and TEG-to-ambient interface via a heat sink (red colour plot) versus the hydrogel (blue colour plot). In a traditional TEG setup with a heat sink, a substantial portion of the ΔT is lost at the interfaces due to thermal impedance, reducing the effective ΔT across the TEG and therefore limiting the power output. The evaporation-enhanced design addresses this by incorporating a hydrogel layer that facilitates evaporative cooling. This allows the temperature in the immediate vicinity of the cold end of the TEG to decrease below the ambient temperature, directly enhancing the ΔT available to the TEG. To determine the extent of cooling by a hydrogel, Fig. 3b shows a thermal image of a hydrogel maintaining a temperature of approximately 20°C compared with the ambient temperature of approximately 30°C, with a modest relative humidity (*RH*) of 40 %. Thus, augmenting a hydrogel to a TEG setup enables us to access a previously inaccessible ΔT across the TEG, significantly contributing to a higher power output. For comparison, Fig. 3c shows the range of power outputs of TEGs compared with the power requirements of various devices, such as wireless devices,

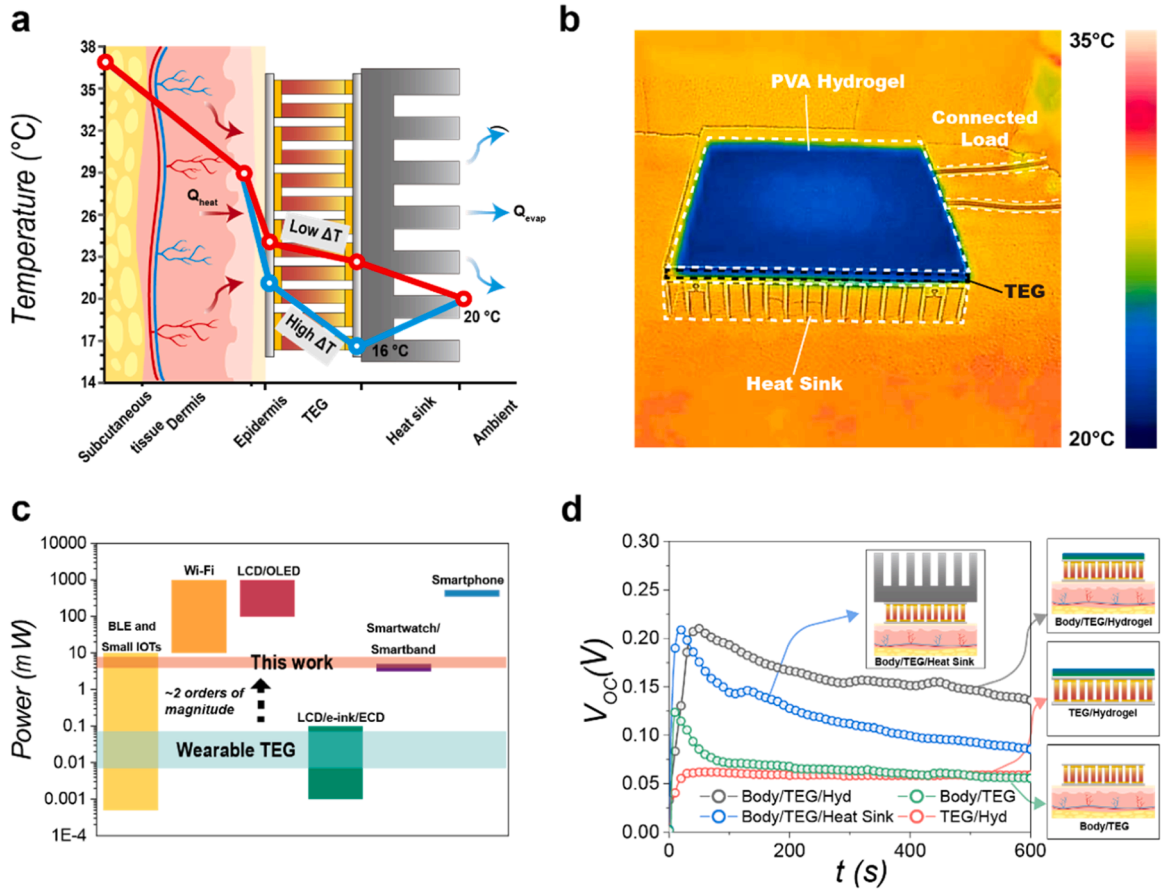

Fig. 3. (a) Temperature profiles across interfaces for traditional (red) and evaporation-enhanced (blue) configurations. (b) Thermal imaging illustrating the hydrogel cooling effect. (c) Comparison of generated power against the consumption requirements of common wearable electronics. (d) Open-circuit voltage V_{OC} evolution for the hydrogel combined system (grey), traditional heat sink (blue), hydrogel evaporation only (red), and body heat only (green).

displays, smartphones, and smartwatches. The power produced by traditional TEGs on human body in the range of 0.01–1 mW is sufficient to power only a small number of sensors and low-power displays. In contrast, the evaporation-enhanced TEG in this work achieves a power output that can power a substantially wider range of electronics and sensors. Fig. 3d further supports these findings, showing a comparison of the open-circuit voltage (V_{oc}), an accurate indicator of the effective ΔT across the TEG, across different setups over time. The evaporation-enhanced TEG (grey plot) consistently outperforms the traditional TEG (blue plot). The green and red plots isolate the contributions of body heat and hydrogel water evaporation, respectively, showing similar magnitudes. Interestingly, the augmented setup achieved in the evaporation-enhanced design provides higher V_{oc} (and therefore ΔT) than the sum of body heat and hydrogel evaporation. This highlights the synergistic effect of the evaporation-enhanced setup in effectively reducing heat loss and therefore enhancing power output.

The efficacy of a hydrogel in lowering the TEG-hydrogel interfacial temperature depends on its water evaporation rate. For a given environmental condition (*RH* or *T*), the rate of water evaporation depends on the microstructure of the hydrogel. In this work, polyvinyl alcohol (PVA) hydrogels were chosen owing to their favourable attributes, such as good water retention, environmental benignity, and microstructures favourable for increasing water evaporation [39,45]. Fig. 4a illustrates the fabrication process involving repeated freeze—thaw (F—T) cycles to form a highly crosslinked, porous structure that enables water transport from the interior of a hydrogel to its surface for sustained evaporation. Fig. 4b, d, f reveals a microscopic porous network critical for water transport. Higher-magnification SEM images (Fig. 4c, e, g) highlight densely entangled PVA fibres forming robust networks that reinforce pore walls. These fibrous and porous features enhance the mechanical integrity and resilience of the hydrogel. In addition, the mechanical strength of PVA hydrogels can be optimized by adjusting the polymer concentration (*wt%*) and the number of freeze—thaw cycles during preparation. For example, lowering the *wt%* improves water absorption but comes at a cost of reduced mechanical robustness. On the other hand, larger pore sizes and higher porosities tend to be observed in low *wt%* samples (Fig. S14), which in turn decreases tortuosity and increases evaporation rates. The mechanical properties of the PVA hydrogel were evaluated via tensile testing (Fig. 4h) and stress (σ) and strain (ε) measurements. The hydrogel exhibited a tensile strength of 0.38 MPa and an elongation at break of 210 %, demonstrating excellent mechanical robustness. This performance enables the hydrogel to withstand deformation and dynamic stress in practical outdoor applications while maintaining structural integrity.

For a given set of realistic environmental parameters (*RH* 40 % and *T* of 26°C), water evaporation from a hydrogel is limited by water diffusion to its surface. Quantitatively, the evaporation rate (*J*) is directly proportional to the water diffusion rate to the evaporating surface and can be correlated with porosity (ϕ) and tortuosity (τ) via (detailed derivation in Note S6):

$$J = -D\frac{\phi}{\tau}\frac{P - P_{air}}{RT\Delta x} \quad (1)$$

where D, P, P_{air}, R, and Δx represent the water vapour diffusion coefficient, vapour pressure, air pressure, gas constant, and hydrogel thickness, respectively.

On the basis of the pore size and porosity data in Fig. S14, the evaporation rate can be determined from Eq. (1). For a given hydrogel

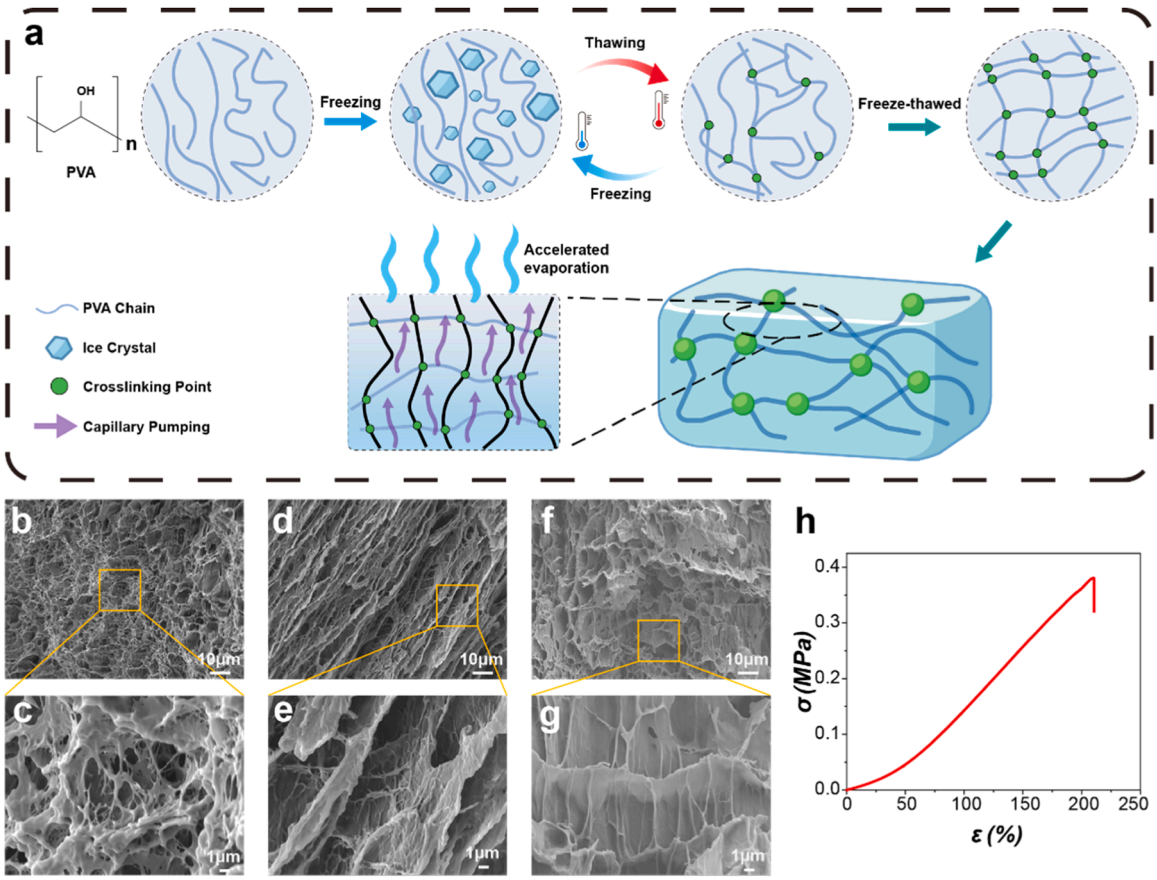

Fig. 4. (a) Schematic of PVA hydrogel preparation by freeze-thaw cycles, in which ice crystals are formed and PVA is crosslinked to form a porous network. This structure aids capillary pumping, enhancing water evaporation. (b, d, f) Low-magnification SEM images of the porous network of the PVA hydrogel (10 μm scale). (b, d, f) High-magnification images detail the pore structure (1 μm scale). (h) Stress–strain curve for the 10 *wt%* PVA-hydrogel.

thickness of 1.0 mm and a composition of 10 *wt%* polymer, a natural evaporation rate as high as 0.62 $kgm^{-2}h$ can be achieved. This is equivalent to 420 Wm^{-2} additional heat flux to be harvested in addition to 50 Wm^{-2} from body heat. This enhancement is substantial and underscores the importance of structural considerations in hydrogel design.

To further explore the limit of enhancing the performance of hydrogel evaporation heat flux, a systematic analysis of the effects of increasing the size of the hydrogel on ΔT and the power output is provided in Fig. 5. To enable accurate comparison, the effects of increasing the evaporation heat flux (through increasing the hydrogel size) on the thermal and electrical performance of the PVA hydrogel-TEG system were investigated under realistic atmospheric conditions (*wind*: 2.8 m s^{-1}, $T = 26°C$, $RH = 40$ %). The detailed fabrication and assembly of the devices are provided in Note S4. Fig. 5a–e present thermal images of PVA hydrogels with dimensions ranging from 4 × 4 cm to 10 × 10 cm, revealing stable ΔTs values between the hydrogel and the environment (ΔT_{Hyd}) at 5.58°C to 5.82°C. This indicates that the temperature decreases within the hydrogel because water evaporation remains relatively consistent across different sizes, which is consistent with the nature of evaporation, which is dependent only on *RH* and *T* [40]. Fig. 5f shows the ΔT across the TEG (ΔT_{TEG}) over time for different hydrogel dimensions, revealing an increase in ΔT_{TEG} with increasing hydrogel size. This is attributed to the higher total evaporation heat flux from larger hydrogels, which enhances the heat flux density and thus the ΔT_{TEG}. To confirm this, Fig. 5g further explores ΔT_{TEG} as a function of *FF*, revealing an increasing trend with decreasing *FF*. A lower *FF* corresponds to a greater ratio of the evaporation area to the active TEG area, which increases the heat flux density and, consequently, ΔT_{TEG}. On the other hand, ΔT_{Hyd} does not change appreciably across different *FFs*, which is consistent with Fig. 5a-e. As expected, the increasing ΔT_{TEG} with increasing hydrogel size or decreasing *FF* directly translates to increased power output and power density (P_D), as shown in Fig. 5h and i. To further support our claim that ΔT_{TEG} originates from evaporation heat flux, Fig. 5j uses computational fluid dynamics (CFD) to simulate ΔT_{Hyd} for a 4 × 4 cm sample, confirming consistency with the experimental results in Fig. 5f. The side and front views of the 4 × 4 cm system, detailing the wind velocity, water vapour mass, and temperature distribution are provided in Fig. 5k. Fig. 5l shows the specific power output per unit weight of the entire setup, showing a similar trend as that in Fig. 5i, which points to the hydrogel's negligible weight compared with that of the TEG. Finally, Fig. 5m in the panel captures the temporal evolution of the cooling effects, showing sustained cooling up to 300 s, highlighting the system's stable and consistent output for continuous energy harvesting.

3. Tuning the fill factor (*FF*)

In addition to increasing heat flux, another equally important tuning knob to maximize the power output of the system is the *FF*. To investigate the impact of *FF* on the thermal and electrical performance of a PVA hydrogel-TEG system in detail, devices consisting of 1–4 TEGs sandwiched with a 10 × 10 cm hydrogel on one side and a 10 × 10 cm aluminum heat sink on the other side were prepared. Fig. 6a – d show schematic illustrations of the configurations corresponding to *FFs* of 0.16, 0.32, 0.48, and 0.64 for devices with 1–4 TEGs, respectively. The corresponding thermal images in Fig. 6e to Fig. 6h, captured under ambient conditions (*wind*: 2.8 m s^{-1}, $T = 26°C$, $RH = 40$ %), reveal

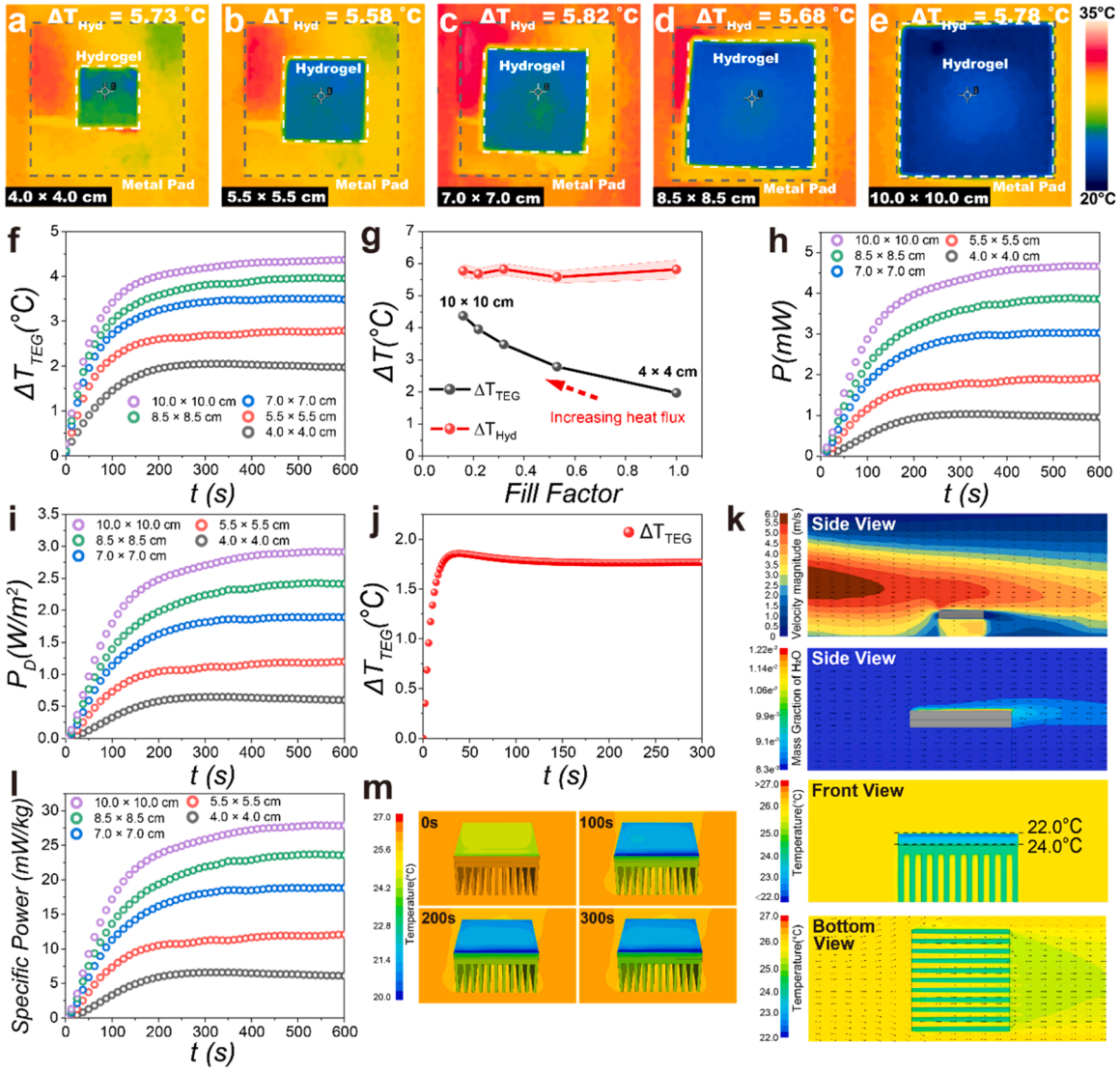

Fig. 5. Thermal and electrical performance analysis. (a–e) Thermal images of PVA hydrogels with dimensions ranging from 4 × 4 cm to 10 × 10 cm under ambient conditions. (f) Temporal evolution of ΔT_{TEG} for varying hydrogel sizes. (g) ΔT_{TEG} as a function of fill factor (FF). (h) ΔT_{TEG} over time for varying hydrogel dimensions, (i) Power density (P_D) over time for different hydrogel dimensions. (j) ΔT_{Hyd} as a function of time for a 4 × 4 cm sample simulated via computational fluid dynamics (CFD). (k) Side, front and bottom views of the wind velocity, water vapour mass, and temperature distribution across the hydrogel-TEG system (4 ×4 cm sample). (l) Specific power output per unit weight of the entire device. (m) Thermal images of the hydrogel-TEG as a function of time, followed by a sustained and consistent cooling effect up to 300 s.

stable ΔT_{Hyd} between the hydrogel and metal pad ranging from 5.84°C to 6.05°C, which is consistent with the results shown in Fig. 5. In Fig. 6i and j, the time profile of ΔT_{TEG} clearly decreases in magnitude with increasing FF. This behavior is attributed to the reduced evaporation area relative to the TEG area at higher *FFs*, which diminishes the heat flux density through the TEG, corroborated by the heat flux trend in Fig. 6k and n.

Interestingly, beyond ΔT_{TEG}, Fig. 6l and m reveal that the actual power output peaks at $FF = 0.48$, which defies classical intuition since a higher *FF* (more TEG materials) is expected to harvest more power. This suggests an optimal balance at $FF = 0.48$, where the trade-off between having a high ΔT_{TEG} and the amount of active TEG materials comes into play. To fundamentally understand this nonmonotonic trend, the framework of effective thermal conductivity laid out by Baranowski *et al.* was introduced [46]. Within a TEG, important heat transport mechanisms, including Fourier conduction, Peltier cooling, and Thomson effects, can be holistically represented by effective thermal conductivity (κ_{eff}). This allows the TEG to be treated as a simple thermal resistor; therefore, the internal thermal impedance can be expressed as:

$$\Theta_{TEG} = \frac{l}{\kappa_{eff} A_{TEG}} \tag{2}$$

where l is the leg height and A_{TEG} is the active thermoelectric area.

For a TEG system in operation, the electrical power output of a TEG is maximized when the internal thermal impedance (Θ_{TEG}) equals the total external thermal impedance of the heat exchangers (Θ_{Hx}). In the context of this work, heat exchanger thermal impedance (Θ_{Hx}) encompasses the aluminum heat sink, the thermal interface between the aluminum heat sink and TEG, and the thermal interface between the TEG and PVA hydrogel. On the other hand, the TEG thermal impedance (Θ_{TEG}) encompasses the effective thermal impedance of the entire TEG module(s). To model the effects of *FF* on ΔT and the power output (P) of the system, the effective thermal impedance can be represented as a function of *FF*, $\Theta_{TEG}(FF) = \Theta_{TEG}/FF$. As such, the power output as a function of *FF* can then be expressed as (details in note S5):

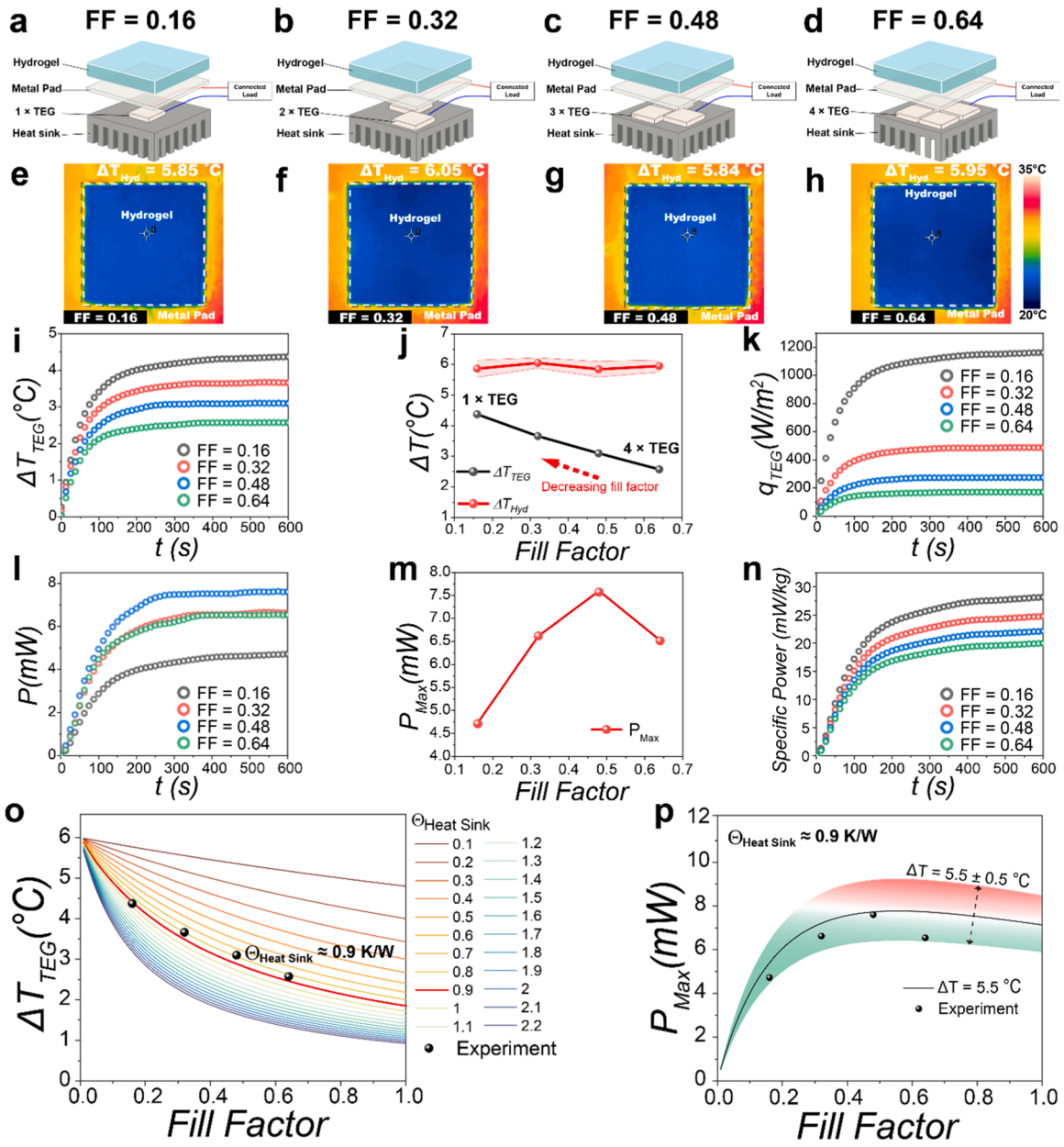

Fig. 6. Impact of *FF* on the Thermal and Electrical Performance of the PVA Hydrogel-TEG System. (a-d) Schematic illustrations of the PVA hydrogel-TEG setup with varying *FF*s of 0.16, 0.32, 0.48, and 0.64, respectively. (e-h) Corresponding thermal images of the setups in (a-d) under ambient conditions (wind: 2.8 m s, T = 26°C, *RH* = 40 %). (i-j) ΔT_{TEG} time profile for different *FF*s (pale red areas indicate standard deviations), showing a decreasing trend with increasing *FF* due to the reduced evaporation area relative to the TEG area, which is consistent with the decreasing heat flux density trend in (k). (l) Power output as a function of time for different *FF*s. (m-n) P_D and specific power time profile as a function of *FF*, with higher values for a lower *FF*. (o) Modelled ΔT_{TEG} as a function of *FF* for varying heat sink thermal impedances (0.2–1.1 K/W). (p) Modelled maximum power density (P_{max}) as a function of *FF* for ΔT_{Hyd} values of 5.5°C ± 0.5°C, showing a peak power output at an *FF* of approximately 0.5.

$$P(FF) = \frac{\Delta T_{supply}^2 \eta_{r,d}}{T_h} \frac{\left(\frac{\Theta_{TEG}}{FF}\right)}{\left(\Theta_{Hx} + \left(\frac{\Theta_{TEG}}{FF}\right)\right)^2} \quad (3)$$

Conceptually, reducing the *FF* from 1.00 increases Θ_{TEG}, which allows the device to maintain a larger fraction of available ΔT across the TEG (ΔT_{TEG}). Importantly, such an increase in Θ_{TEG} brought the system closer to thermal impedance matching with Θ_{Hx}. However, when the *FF* is too low, the power output also decreases because of the combined effect of fewer TEG materials and a thermal impedance mismatch ($\Theta_{TEG} > \Theta_{Hx}$). In Fig. 6m, a peak is observed at *FF* = 0.48, suggesting that such a configuration approaches thermal impedance matching ($\Theta_{TEG} = \Theta_{Hx}$). This observation underscores the importance of carefully tuning the *FF* to achieve optimal performance in hydrogel-TEG systems.

To holistically visualize the interplay between ΔT_{TEG}, *FF*, and power output, Fig. 6o shows the models of ΔT_{TEG} as a function of *FF* for varying heat sink thermal impedances (0.2–1.1 K/W). It is evident that ΔT_{TEG} increases with decreasing *FF* for a given thermal impedance. This aligns with experimental trends, highlighting the role of thermal impedance in modulating the effective ΔT across the TEG. Importantly, for a known ΔT_{Supply}, $\Theta_{TEG}(FF)$, and Θ_{TEG}, fitting parameters from various *FF*s can be used to determine Θ_{Hx}, which is otherwise a complex parameter to be experimentally measured. Finally, Fig. 6p models the maximum power density (P_{max}) for ΔT_{Hyd} values of 5.5°C ± 0.5°C, predicting a peak at an *FF* of approximately 0.5, similar to the experimental observations. This consistency between the modelled and measured results emphasizes the importance of optimizing *FF* to maximize energy harvesting efficiency in

hydrogel-TEG systems, providing a pathway for designing more effective ambient energy harvesting devices that use fewer materials and are therefore thinner and lighter.

4. Conclusion

In this study, we demonstrated an evaporation-enhanced approach to overcome the longstanding limitations of thermal impedance matching in thermoelectric generators (TEGs). As a proof of concept, the integration of bodily heat flux with the hydrogel-based evaporative enthalpy enables thermal impedance matching between skin and TEG. Synergistically, this also result in less material utilization yet higher power output. Our findings challenge conventional design paradigms that often equate higher material usage with improved performance. Importantly, the strategy employed in this work bypasses the reliance on external thermal inputs or sunlight, unlike many hydrovoltaics or photothermal systems. Technologically, this advancement is relevant for autonomous, multifunctional wearable devices for continuous health and environmental monitoring.

In terms of implementation into wearable devices, it is worth noting that a further improvement to counter the water lost to support continuous evaporation remains a critical challenge that needs to be overcome. For instance, potential advances could involve an integrated water reservoir or leveraging sweat to provide a continuous liquid source for evaporation. For instance, future integration with sweat-wicking could enable indefinite operation [47]. Beyond thermoelectrics, the insights derived from this work can be applied to other areas such as solid-state batteries, which suffer from interfacial thermal resistances that limit ion transport and cause localized heating.

5. Experimental section

5.1. Synthesis of the PVA hydrogel

Polyvinyl alcohol (PVA, $M_w = 1750 \pm 50$) was purchased from Sinopharm Chemical Reagent Co., Ltd. Polyvinyl alcohol (PVA) hydrogels were synthesized via the standard freeze—thaw (F-T) method to form a physically crosslinked porous network. The PVA powder (average $M_w = 1750 \pm 50$) was dissolved in deionized (DI) water at a concentration of 10 *wt%*. The solution was heated and continuously stirred at 90 °C for 40 min to obtain a clear and homogeneous solution. Then, the hot solution was cooled to room temperature. Next, the solution was poured into flat molds to control the thickness at approximately 1 mm before moving forward during the F–T cycles. The molds were subsequently transferred to a freezer at –30 °C for 8 h for ice crystal formation, which induced phase separation and forced the PVA chains to aggregate. The frozen PVA solutions were then thawed at ambient temperature (~25 °C) for 2 h to allow complete melting of the ice. This F-T process was repeated for a total of four cycles to achieve sufficient crosslink density and mechanical integrity. The hydrogel samples were immersed in DI water for at least 48 h to reach equilibrium before use. The hydrogels were cut into different sizes (4.0 × 4.0 cm, 5.5 × 5.5 cm, 7.0 × 7.0 cm, 8.5 × 8.5 cm, and 10.0 × 10.0 cm) for further experimental characterization.

5.2. Materials characterization

The internal structure of the PVA hydrogel was characterized via a JEOL 7800 F field emission scanning electron microscope (FE-SEM) under high vacuum. Before SEM imaging, the PVA hydrogel samples were frozen rapidly in liquid nitrogen to preserve the native microstructure and then immediately transferred for freeze-drying to remove the remaining water content without collapsing the porous network. Gold-sputtering was subsequently performed on the cross-sections of the resulting freeze-dried samples to ensure conductivity and prevent charging during SEM imaging. During operation, the real-time surface temperatures of the hydrogel-TEG systems were characterized via an infrared thermal imaging camera (FLIR AX8), which provides the spatially resolved temperature of the hydrogel under experimental conditions. The mechanical properties of the PVA hydrogels were characterized via tensile testing via a universal material testing machine (CMT5105, MTS Systems). Rectangular hydrogel samples were tested at a strain rate of 10 mm/min. The stress–strain curves were recorded, and the tensile strength and elongation at break were extracted to evaluate the mechanical integrity.

5.3. Hydrogel-enhanced TEG device fabrication and assembly

The evaporation-enhanced TEG devices used in this work consisted of commercial TEG modules (TES1–24125, Everredtronics Ltd.), each with lateral dimensions of 40 mm × 40 mm and a thickness of 4 mm. FF = 0.16, 0.32, 0.48, and 0.64 devices consist of 1, 2, 3, and 4 TEG modules, respectively. These modules were electrically connected in series via low-resistance solder with correct polarity matching. Aluminium heat sinks (100 mm × 100 mm × 10 mm) were adhered to the hot side of the TEGs via low-thermal-resistance thermal interface materials from Shin-Etsu (X-23–7921–5; thermal resistance: 5.8 mm2·K/W) to ensure effective thermal conduction with the ambient environment. For the cold side, aluminium plates (100 mm × 100 mm × 0.3 mm) were adhered to the TEGs via the same thermal interface materials. The 10 wt% PVA hydrogel films (prepared via four freeze–thaw cycles, as shown in Fig. 4) were placed in direct contact with the aluminum surface to facilitate evaporative cooling. The hydrogels were saturated with deionized water prior to assembly to ensure continuous water availability for further evaporation tests.

5.4. Relative humidity and temperature setup

To control the experimental atmospheric conditions, all the experiments were carried out in an enclosed acrylic environment (1200 mm × 800 mm × 800 mm). To ensure precise control of the *RH*, a dehumidifier (Dometic HD30AR 30 L) and a humidifier (Mijia humidifier 2) were adopted to achieve dynamic equilibrium. For ambient temperature control, a portable air conditioner (1100 W cooling capacity and 800 W heating capacity) was used. A temperature and humidity sensor (UT333, from UNI-T) was adopted for accurate readings of relative humidity and temperature after humidity calibration in a glovebox. For thermal insulation during the experiment, a polystyrene block was used to place the hydrogel-enhanced TEG device. The enclosed experimental setup is illustrated in Fig. S15. A vane probe anemometer from RS Pro (193–8696) was used to measure the wind speed. For the surface temperature of the hydrogel, an FLIR AX8 thermal camera was used to study the time evolution of the temperature profiles of the surrounding air. The temperature data were extracted from the center of the hydrogel with autogain correction applied.

5.5. Electrical measurements and device applications

To measure the open-circuit voltage (V_{OC}) and output power (P) of the hydrogel-enhanced TEG devices, the system was connected in series to a precision electronic load (KEL 102). The voltage was measured via a Keithley 2100 multimeter. Both instruments were controlled via the LabVIEW program. For the V_{OC} measurements, the KEL 102 resistance was set to its maximum value (7500 Ω) to achieve negligible current flow. To obtain P–R curves, the load resistance was swept from 1 Ω to 1000 Ω. In addition, to demonstrate applications, a system comprising an evaporation-enhanced TEG setup, a nanopower managing unit, a wireless environment sensing unit (ambient light sensor, temperature sensor, humidity sensor and ambient pressure sensor) and a signal receiver (see Note S3 for details) was constructed. The sensing unit powers the electricity generator via a stepped-up voltage, sending out environmental data wirelessly through Bluetooth low-energy (BLE)

advertisement packets to the receiver for data logging. Using the 10 × 10 cm PVA hydrogel-TEG setup, four sensors were energized simultaneously over a 24-hour period where key environmental parameters, including light intensity, humidity, temperature, and atmospheric pressure, were monitored. These data reveal the robustness of the hydrogel-enhanced generator throughout the day and night. The system maintains stable performance despite substantial variations in humidity (20–60 %), temperature (10–35 °C), and light intensity.

CRediT authorship contribution statement

Jinfeng Dong: Writing – review & editing, Investigation. **Jing Cao:** Writing – review & editing, Writing – original draft, Conceptualization. **Soe Ko Ko Aung:** Investigation. **Sai Kishore Ravi:** Investigation. **Zichen Gong:** Writing – review & editing, Writing – original draft, Methodology, Investigation, Formal analysis, Data curation, Conceptualization. **Ady Suwardi:** Writing – review & editing, Writing – original draft, Investigation, Funding acquisition, Formal analysis, Data curation, Conceptualization. **Zhaogang Dong:** Investigation. **Yujie Ke:** Investigation. **Bhuvanesh Srinivasan:** Investigation. **Tosawat Seetawan:** Investigation. **Surasak Ruamruk:** Investigation. **Thang Bach Phan:** Investigation. **Qi Qian:** Investigation.

Declaration of Competing Interest

The authors declare that they have no known competing financial interests or personal relationships that could have appeared to influence the work reported in this paper.

Acknowledgements

We acknowledge BroadTech Engineering Pte. Ltd. for computational fluid dynamics (CFD) simulations. A.S. acknowledges funding in part by project #RNE-p3-24 of the Shun Hing Institute of Advanced Engineering, direct grant 4055224, and startup funding from The Chinese University of Hong Kong. J.C., T.S., and S.R. acknowledge funding from e-Asia Joint Research Program award no. R22I1IR053 and LCER Phase 2 ETGC award no. U2411D4011. B.S. & J.C. thank the Anusandhan National Research Foundation (ANRF/erstwhile SERB) for funding the ASEAN-India project (CRD/2024/000912).

Appendix A. Supporting information

Supplementary data associated with this article can be found in the online version at doi:10.1016/j.nanoen.2026.111780.

Data availability

Data will be made available on request.

References

[1] D.S. Yang, R. Ghaffari, J.A. Rogers, Sweat as a diagnostic biofluid, Science 379 (2023) 760–761.
[2] Y. Luo, M.R. Abidian, J.-H. Ahn, D. Akinwande, A.M. Andrews, M. Antonietti, Z. Bao, M. Berggren, C.A. Berkey, C.J. Bettinger, Technology roadmap for flexible sensors, ACS Nano 17 (2023) 5211–5295.
[3] J. Kim, A.S. Campbell, B.E.-F. de Ávila, J. Wang, Wearable biosensors for healthcare monitoring, Nat. Biotechnol. 37 (2019) 389–406.
[4] R.T. Arwani, S.C.L. Tan, A. Sundarapandi, W.P. Goh, Y. Liu, F.Y. Leong, W. Yang, X. T. Zheng, Y. Yu, C. Jiang, Stretchable ionic–electronic bilayer hydrogel electronics enable in situ detection of solid-state epidermal biomarkers, Nat. Mater. 23 (2024) 1115–1122.
[5] S. Hong, Y. Gu, J.K. Seo, J. Wang, P. Liu, Y.S. Meng, S. Xu, R. Chen, Wearable thermoelectrics for personalized thermoregulation, Sci. Adv. 5 (2019) eaaw0536.
[6] J. Kim, S. Khan, P. Wu, S. Park, H. Park, C. Yu, W. Kim, Self-charging wearables for continuous health monitoring, Nano Energy 79 (2021) 105419.
[7] S. Khan, J. Kim, T.-U. Kang, G. Park, S. Lee, J.-W. Park, W. Kim, Compact vital-sensing band with uninterrupted power supply for core body temperature and pulse rate monitoring, ACS Sens. 9 (2024) 5885–5895.
[8] N. Brasier, J. Wang, W. Gao, J.R. Sempionatto, C. Dincer, H.C. Ates, F. Güder, S. Olenik, I. Schauwecker, D. Schaffarczyk, Applied body-fluid analysis by wearable devices, Nature 636 (2024) 57–68.
[9] L. Liang, X. Liu, P. Li, W. Wang, N. Kuang, Y. Zhang, Y. Kang, G. Yao, Z. Huang, C. Zhou, A wearable multimodal health monitoring bracelet powered by high-power-density flexible thermoelectric generators, Device (2025).
[10] L. Yin, K.N. Kim, A. Trifonov, T. Podhajny, J. Wang, Designing wearable microgrids: towards autonomous sustainable on-body energy management, Energy Environ. Sci. 15 (2022) 82–101.
[11] B. Tian, H. Ma, X. An, Y. Mao, Q. Deng, Q. Sun, R. Ang, Multifunctional durable solid-state thermoelectric sensor enabled by interstitial Co doping in Mg3 (Sb, Bi), Device 2 2 (2024).
[12] W. Chen, X.-L. Shi, M. Li, T. Liu, Y. Mao, Q. Liu, M. Dargusch, J. Zou, G.Q. Lu, Z.-G. Chen, Nanobinders advance screen-printed flexible thermoelectrics, Science 386 (2024) 1265–1271.
[13] A.-H. Cavusoglu, X. Chen, P. Gentine, O. Sahin, Potential for natural evaporation as a reliable renewable energy resource, Nat. Commun. 8 (2017) 617.
[14] R.F. Service, Hydrovoltaics' tap energy from ubiquitous moisture, American Association for the Advancement of, Science (2024).
[15] H. Wang, Y. Sun, T. He, Y. Huang, H. Cheng, C. Li, D. Xie, P. Yang, Y. Zhang, L. Qu, Bilayer of polyelectrolyte films for spontaneous power generation in air up to an integrated 1,000 V output, Nat. Nanotechnol. 16 (2021) 811–819.
[16] Z. Zhang, X. Li, J. Yin, Y. Xu, W. Fei, M. Xue, Q. Wang, J. Zhou, W. Guo, Emerging hydrovoltaic technology, Nat. Nanotechnol. 13 (2018) 1109–1119.
[17] J. Xu, P. Wang, Z. Bai, H. Cheng, R. Wang, L. Qu, T. Li, Sustainable moisture energy, Nat. Rev. Mater. (2024), https://doi.org/10.1038/s41578-023-00643-0.
[18] I. Mathews, S.N. Kantareddy, T. Buonassisi, I.M. Peters, Technology and market perspective for indoor photovoltaic cells, Joule 3 (2019) 1415–1426.
[19] X. Zhang, K. Ahmad, Z. Almutairi, C. Wan, Hydro-thermoelectric generators for harvesting heat and moisture from the human body for powering wearable electronics, Device (2025).
[20] F. Suarez, A. Nozariasbmarz, D. Vashaee, M.C. Öztürk, Designing thermoelectric generators for self-powered wearable electronics, Energy Environ. Sci. 9 (2016) 2099–2113.
[21] Q. Yang, S. Yang, P. Qiu, L. Peng, T.-R. Wei, Z. Zhang, X. Shi, L. Chen, Flexible thermoelectrics based on ductile semiconductors, Science 377 (2022) 854–858, https://doi.org/10.1126/science.abq0682.
[22] S. Xu, S. Horta, A. Lawal, K. Maji, M. Lorion, M. Ibáñez, Interfacial bonding enhances thermoelectric cooling in 3D-printed materials, Science 387 (2025) 845–850, https://doi.org/10.1126/science.ads0426.
[23] S. Ghosh, A. Nozariasbmarz, H. Lee, L. Raman, S. Sharma, R.B. Smriti, D. Mandal, Y. Zhang, S.K. Karan, N. Liu, High-entropy-driven half-Heusler alloys boost thermoelectric performance, Joule 8 (2024) 3303–3312.
[24] D. Song, C. Zhao, B. Chen, W. Ma, K. Wang, X. Zhang, Conveyor mode enabling continuous ionic thermoelectric conversion, Joule 8 (2024) 3217–3232.
[25] J. Cheng, W. Xue, T. Zhang, X. Li, Y. Zhu, L. Yin, H. Yao, Z. Fu, L. Wu, C. Chen, A universal approach to high-performance thermoelectric module design for power generation, Joule 9 (2025).
[26] D. Zhang, N. Ngoh Yen Qi, S. Faye Duran Solco, X. Li, A. Suwardi, Lattice architectures for thermoelectric energy harvesting, ACS Energy Lett. 9 (2024) 2240–2247.
[27] X.Y. Tan, H. Liu, J. Dong, A.C.Y. Ngo, A. Suwardi, J. Cao, Thermoelectrics for nuclear fusion reactors: opportunities and challenges, J. Mater. Chem. A 12 (2024) 17771–17792.
[28] D. Zhang, J. Ramiah, M. Cagirici, K. Saglik, S.F.D. Solco, J. Cao, J. Xu, A. Suwardi, Thermoelectric nanowires for dense 3D printed architectures, Mater. Horiz. 11 (2024) 847–854.
[29] S. Choo, J. Lee, B. Şişik, S.-J. Jung, K. Kim, S.E. Yang, S. Jo, C. Nam, S. Ahn, H. S. Lee, Geometric design of Cu2Se-based thermoelectric materials for enhancing power generation, Nat. Energy 9 (2024) 1105–1116.
[30] S. Roychowdhury, T. Ghosh, R. Arora, M. Samanta, L. Xie, N.K. Singh, A. Soni, J. He, U.V. Waghmare, K. Biswas, Enhanced atomic ordering leads to high thermoelectric performance in AgSbTe2, Science 371 (2021) 722–727.
[31] P. Zhao, W. Xue, Y. Zhang, S. Zhi, X. Ma, J. Qiu, T. Zhang, S. Ye, H. Mu, J. Cheng, Plasticity in single-crystalline Mg3Bi2 thermoelectric material, Nature 631 (2024) 777–782.
[32] H. Hu, Y. Ju, J. Yu, Z. Wang, J. Pei, H.-C. Thong, J.-W. Li, B. Cai, F. Liu, Z. Han, Highly stabilized and efficient thermoelectric copper selenide, Nat. Mater. 23 (2024) 527–534.
[33] J. Dong, Y. Liu, Z. Li, H. Xie, Y. Jiang, H. Wang, X.Y. Tan, A. Suwardi, X. Zhou, J.-F. Li, High thermoelectric performance in rhombohedral GeSe-LiBiTe2, J. Am. Chem. Soc. 146 (2024) 17355–17364.
[34] J. Dong, A. Suwardi, X.Y. Tan, N. Jia, K. Saglik, R. Ji, X. Wang, Q. Zhu, J. Xu, Q. Yan, Challenges and opportunities in low-dimensional thermoelectric nanomaterials, Mater. Today 66 (2023) 137–157.
[35] B. Jiang, W. Wang, S. Liu, Y. Wang, C. Wang, Y. Chen, L. Xie, M. Huang, J. He, High figure-of-merit and power generation in high-entropy GeTe-based thermoelectrics, Science 377 (2022) 208–213.
[36] X. Zhang, H. Zhu, X. Dong, Z. Fan, Y. Yao, N. Chen, J. Yang, K. Guo, J. Hao, L. He, High-performance MgAgSb/Mg3 (Sb, Bi) 2-based thermoelectrics with η= 12% at T≤ 583K, Joule 8 (2024) 3324–3335.
[37] D. Mao, Y. Zhou, Y. Yu, Y. Wang, M. Han, Q. Meng, Y. Lu, J. Feng, M. Kong, H. Yang, Scalable and sustainable manufacturing of twin boundary-enhanced flexible Bi0. 4Sb1. 6Te3 films with high thermoelectric performance, Joule 8 (2024) 3313–3323.

[38] L. Miao, S. Zhu, C. Liu, J. Gao, Z. Zhang, Y. Peng, J.-L. Chen, Y. Gao, J. Liang, T. Mori, Comfortable wearable thermoelectric generator with high output power, Nat. Commun. 15 (2024) 8516.
[39] Z. Gong, A. Suwardi, J. Cao, Electricity generation from ambient water evaporation in the absence of sunlight via PVA-based porous hydrogels, Adv. Funct. Mater. (2025) 2423371.
[40] J. Cao, J. Dong, J. Wu, A. Suwardi, Evapolectrics: direct harvesting of electricity from evaporation using thermoelectrics, ACS Nano 19 (2025) 26249–26258, https://doi.org/10.1021/acsnano.5c10693.
[41] N. He, H. Wang, F. Li, B. Jiang, D. Tang, L. Li, Ion engines in hydrogels boosting hydrovoltaic electricity generation, Energy Environ. Sci. 16 (2023) 2494–2504.
[42] G. Park, H. Park, J. Seo, J.C. Yang, M. Kim, B.J. Lee, S. Park, Bidirectional thermo-regulating hydrogel composite for autonomic thermal homeostasis, Nat. Commun. 14 (2023) 3049.
[43] P. Zhang, Z. Li, Y. Wang, W. Sun, K. Zhu, Q. Li, B. Li, Z. Wang, K. Wang, Z. Zheng, Electronic skin with biomimetic structures realizes excellent isothermal regulation, Nano Energy 121 (2024) 109189.
[44] G. Xue, Y. Xu, T. Ding, J. Li, J. Yin, W. Fei, Y. Cao, J. Yu, L. Yuan, L. Gong, Water-evaporation-induced electricity with nanostructured carbon materials, Nat. Nanotechnol. 12 (2017) 317–321.
[45] X. Zhou, F. Zhao, Y. Guo, Y. Zhang, G. Yu, A hydrogel-based antifouling solar evaporator for highly efficient water desalination, Energy Environ. Sci. 11 (2018) 1985–1992.
[46] L.L. Baranowski, G. Jeffrey Snyder, E.S. Toberer, Effective thermal conductivity in thermoelectric materials, J. Appl. Phys. 113 (2013).
[47] J. Son, G.Y. Bae, S. Lee, G. Lee, S.W. Kim, D. Kim, S. Chung, K. Cho, Cactus-spine-inspired sweat-collecting patch for fast and continuous monitoring of sweat, Adv. Mater. 33 (2021) 2102740.